Influence of Thermally-Induced Structural Transformations over Magnetic and Luminiscence Properties of Tartrate-based Chiral Lanthanide Organic-Frameworks

Uxua Huizi-Rayo,[a] Andoni Zabala-Lekuona,[a] Alessio Terenzi,[b,c] Carlos M. Cruz,[d] Juan M. Cuerva,[d] Antonio Rodríguez-Diéguez,[e] Jose Angel García,[f] José M. Seco,[a] Eider San Sebastian[a] and Javier Cepeda[a],*

This work reports on the synthesis and characterization of five enantiomeric pairs of isostructural 3D metal-organic frameworks (MOFs) with the general formula {[Ln$_2$(μ_4-tar)$_2$(μ-tar)(H$_2$O)$_2$]·xH$_2$O}$_n$ [where Ln(III) = Tb (**Tb-L** and Tb-D), Dy (**Dy-L** and **Dy-D**), Ho (**Ho-L** and **Ho-D**), Er (**Er-L** and **Er-D**) and Tm (**Tm-L** and **Tm-D**); tar = tartrate (D- or L-) and x = 3 or 4 depending on the counterpart] that present with interesting luminescence and magnetic properties. These MOFs under-go progressive and reversible dehydration processes upon controlled heating yielding three crystalline phases (**Ln-L'**, **Ln-L''** and **Ln-L'''**). Alternating current magnetic measurements on Tb, Dy and Er-based compounds exhibit field induced single-molecule magnet behavior dominated by QTM, which is partially suppressed when diluted on a Y-based matrix. Tartrate ligands show poor room temperature sensitization of Tb and Dy centers that is enhanced at low temperature (10 K), even enabling weak Tm-based emission. More interestingly, the dehydration modulates both magnetic and photoluminescent properties on the basis of both the distortions occurring in the coordination shells and decrease of water molecules acting as quenchers, respectively, imbuing these materials with potential humidity sensing capacity. Remarkably, the Tb-based MOF shows circularly polarized luminescence (CPL), being one of the examples of this very scarce family of CPL emitters reported so far.

Introduction

Metal-organic frameworks (MOFs) have attracted an increasing interest of researchers working in the field of multifunctional materials due to their structural and topological diversity, as well as the properties that arise from their structural features.[1] This is a result of the endless combinations of metal centers and organic ligands, which provides MOFs with the possibility of being synthesized with the desired functionalities by following the foundations set by the reticular chemistry.[2] Though it is true that potential porosity has traditionally been the most sought property given its implication in processes such as gas adsorption and separation,[3] drug or biomolecule release,[4] heterogeneous catalysis,[5] ionic conductivity[6] and crystallization templates,[7] other functionalities including magnetism and photoluminescence (PL) have also caused an important scientific impact.[8] In particular, the study of magnetic properties has recently focused on single-molecule magnets (SMMs) since they are revolutionizing cutting-edge technologies with applications for magnetic information storage, magneto-optics and molecular spintronics.[9] Since On the other hand, the growth of MOFs showing PL has been launched during the last decade owing to their large applicability as enhanced solid-state photodevices (OLEDs, LLPs and so on)[10] as well as molecular sensors.[11] In this context, the use of Ln(III) ions as metal centers yielding novel MOFs has been multiplied due to not only their large and flexible coordination geometry but also to their unique magnetic and luminescent properties derived from their shielded 4f electron shell.[12] As corroborated in 2014 by Mínguez-Espallargas et al. with the first reported Ln(III)-based MOF showing SMM behavior,[13] these paramagnetic centers afford a large magnetic moment and significant single-ion anisotropy derived from spin–orbit coupling,[14] which depending on their local environment, may lead to large barriers for the reversal of the magnetization.[15] Regarding their luminescence performance, it should be pointed out that lanthanide-organic frameworks (LnOFs) present intense, narrow and long-lived emission bands covering the near-infrared and visible regions arising from the intraionic *f–f* transitions.[16] Despite the low absorption coefficients associated to

a *Departamento de Química Aplicada, Facultad de Química, Universidad del País Vasco (UPV/EHU), 20018 Donostia, Spain. E-mail: javier.cepeda@ehu.es*

b *Donostia International Physics Center, Paseo Manuel de Lardizabal 4, 20018, Donostia, Spain.*

c *Dept. of Biological, Chemical and Pharmaceutical Sciences and Technologies, University of Palermo, Viale delle Scienze, Ed. 17, 90128 Palermo, Italy.*

d *Dept. of Organic Chemistry, UEQ, C/ Severo Ochoa s/n, University of Granada, 18071, Granada, Spain.*

e *Dept. of Inorganic Chemistry, C/ Severo Ochoa s/n, University of Granada, 18071, Granada, Spain.*

f *Departamento de Física Aplicada II, Facultad de Ciencia y Tecnología, Universidad del País Vasco/Euskal Herriko Unibertsitatea (UPV/EHU), 48940, Leioa, Spain.*

† *Electronic Supplementary Information (ESI) available: materials & measurements, SCXR and PXRD data collection, structural details, synthesis, CShMs, thermogravimetry, IR measurements, magnetic properties, DFT calculations, PL measurements and circular dichroism and circularly polarized luminescence. See DOI: 10.1039/x0xx00000x.*

ARTICLE

these transitions, lanthanide coordination to ligands may yield an efficient ligand-to-metal energy transfer and bring a bright emission by means of the well-known antenna effect.[17] Taking into account that this effect nurtures from the metal-ligand bond strength, ligands containing carboxylate linkers are appropriate given the large coordination capacity of those moieties.[18]

In addition to the previous considerations, the occurrence of a chiral crystal structure opens the way to other less explored physical phenomena related to the intriguing interaction of these solids with electromagnetic fields, where left- and right-handed structures tend to manifest opposed effects,[19] which are useful and applied in non-linear optics and magnetic materials.[20] In particular, circularly polarized luminescence (CPL) has intriguing applications in spintronics,[21] quantum computation,[22] and optical data storage.[23] Furthermore, it can be also used to induce exotic quantum phenomena such as the Floquet topological state,[24] as well as in other fields such as chirality sensing[25] and enhanced image contrast for advanced medical imaging technologies.[26] In all cases, applicability of CPL demands a large value of the dissymmetry factor (g_{lum}), which is challenging since the mechanisms governing the chiroptical response are still somewhat obscure.[27] It is interesting to note that most of the materials reported so far showing CPL properties are based on organic molecules, whereas the examples based on hybrid metal-organic materials are scarce[28]. Still, it seems that the latter hybrid materials can undoubtedly boost an enhanced performance by incorporating heavy atoms such as lanthanides(III).[29] Moreover, it is important to underline that studies on chiral MOFs showing SMM behavior are rather scarce mainly because control of chirality is not an easy task.[30]

We herein report the synthesis and structural, optical and magnetic characterization of five isostructural enantiomeric pairs of 3D microporous MOFs based on Ln(III) ions and either D- or L-tartrate ligand, namely **Tb-L, Tb-D, Dy-L, Dy-D, Ho-L, Ho-D, Er-L, Er-D, Tm-L, Tm-D**. These MOFs present intriguing chiral luminescence and magnetic properties besides tunable by thermal activation processes.

Results and discussion

Comments on the synthesis of compounds

Five pairs of enantiomerically pure MOFs of general formula [Ln$_2$(L/D-tart)$_3$(H$_2$O)$_3$]·xH$_2$O}$_n$ (where Ln = Tb(III), Dy(III), Ho(III), Er(III) or Tm(III) and L/D-tart = L- or D-tartrate) have been synthesized under hydrothermal conditions following the general procedure described in the Experimental Section. The so-generated compounds have been obtained as single crystals and all crystal structures solved. It must be noticed that no racemization was observed during reaction despite what previously observed for other previous reports on chiral compounds.[31]

Structural description of {[Ln$_2$(μ_4-tar)$_2$(μ-tar)(H$_2$O)$_2$]·xH$_2$O}$_n$ [where Ln(III) = Tb, Dy, Ho, Er and Tm; x = 3-4]

The synthesized MOFs crystallize in the non-enantiogenic P1 space group in such a way that 3D open framework containing microchannels retains the chirality afforded by L-/D-tartate ligands. The analysis of the X-ray diffraction data reveals the isostructural nature of all five pairs of compound, with some expected slight differences (see below).

The asymmetric unit is comprised by two crystallographically independent Ln(III) ions [Ln(1) and Ln(2)], three tartrate ligands, two coordination water molecules and four/five lattice water molecules. Both Ln(III) atoms (Tb, Dy, Ho, Er) are nine coordinated species, with eight oxygen donor atoms from three tartrate dianionic ligands (six carboxylate and two hydroxyl oxygen atoms) and one additional oxygen donor atom provided by a coordinated water molecule [Ln(O$_{carb}$)$_6$(O$_{hid}$)$_2$(O$_w$)$_1$] (see Figure 1). The crystal structure subtly adapts bond distances and coordination modes to the progressive decrease of the Ln(III) ion size, as previously observed for other lanthanide based families.[32] Remarkably, the decrease of the Ln(III) ion size brings clear-cut change for thulium(III), where Tm2 atoms are forced to drop their coordination number to eight in order to overcome the steric hindrance in the sphere (see Figure 1 and ESI for further details).

Continuous shape measurements (CShMs)[33] revealed that despite their equivalent coordination, Ln1 and Ln2 atoms build different polyhedra, resembling capped square antiprisms (CSAPR) and muffins (MFF), respectively, in Tb, Dy, Ho and Er-based compounds (see Figure 1 and Tables S11–13 for other reported compounds), whereas Tm2 builds an 8-vertices biaugmented trigonal prism (BTPR). It is worth noticing that moving from Tb(III) to Er(III), coordination polyhedra around Ln1 become progressively less distorted and more similar to CSAPR whereas the opposed trend is observed for Ln2 environments (but Tm2).

ARTICLE
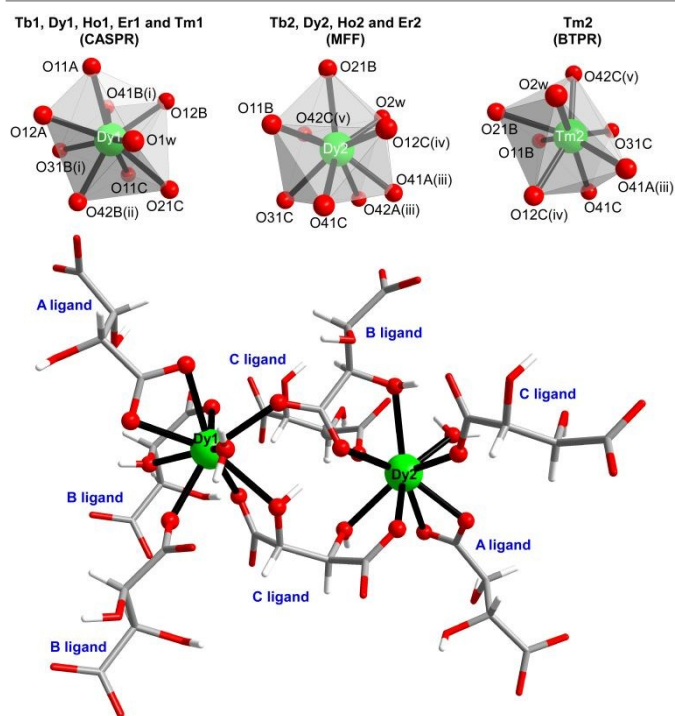
Figure 1. Excerpt of the crystal structure of compound **Dy-L** showing the coordination polyhedra for Dy1 and Dy2, as well as the particular case of the coordination mode and polyhedron for Tm2. Symmetries: (i) x, 1 + y, z; (ii) − 1 + x, 1 + y, z; (iii) − 1 + x, − 1 + y, − 1 + z; (iv) x, − 1 + y, z; (v) 1 + x, y, z; (vi) x, − 1 + y, z.

Coordination bond lengths vary in the 2.29–2.80 Å range (Tables S3–5 in ESI, shorter for Tm2), in agreement with data reported for other LnOFs,[2b,39,52b] where both limit distances correspond to the shell of Ln2 atoms in agreement with their aforementioned large distortion. In most of structures (compounds **Tb**–**Er**), tartrate ligands show two different coordination modes. One of the tartrate ligands (A ligand in Figure 1) displays the bis(bidentate) μ-$\kappa^2O,O':\kappa^2O'',O'''$ mode, whereas two tartrate ligands (B and C) display a hexadentate μ_4-$\kappa O:\kappa^2O',O'':\kappa^2O''',O'''':\kappa O'''''$ mode that exerts two five-member chelating rings involving a carboxylate and a hydroxyl oxygen atom. Instead, in Tm compounds, the A tartrate ligand is forced to acquire the bridging μ-$\kappa^2O,O':\kappa O''$ mode owing to the reduced coordination index shown by Tm2 atom. The porous nature of these flexible MOFs allows them to acquire a variable number of lattice water molecules, which brings small changes in the hydrogen bonding scheme. All the bridges imposed by tartrate ligands among neighboring Ln(III) atoms yields a 3D framework that may be described with the **fsx** topology since it possesses the $(4^2 \cdot 6^4)(4^2 \cdot 6^7 \cdot 8)$ point symbol, taking into account that Ln(III) and μ_4-tar ligands act as 5- and 4-connected nodes (Figure 2).[34] The growth of this structure leaves narrow microchannels along the crystallographic [001] direction that correspond to the ca. 13.5% of the unit cell volume and are occupied by crystallization water

molecules.[35] The latter are involved in a very intricate hydrogen bonding scheme in which they form infinite supramolecular chains that get anchored to the framework through hydrogen bonding interactions with hydroxyl groups and coordination water molecules (see Tables S6–10 in ESI). In those cases where the content of lattice water molecules is lower (three water molecules per formula unit in **Ho-D** and **Er-D**) the hydrogen bonding pattern is slightly modified (see Figure S3 in ESI).
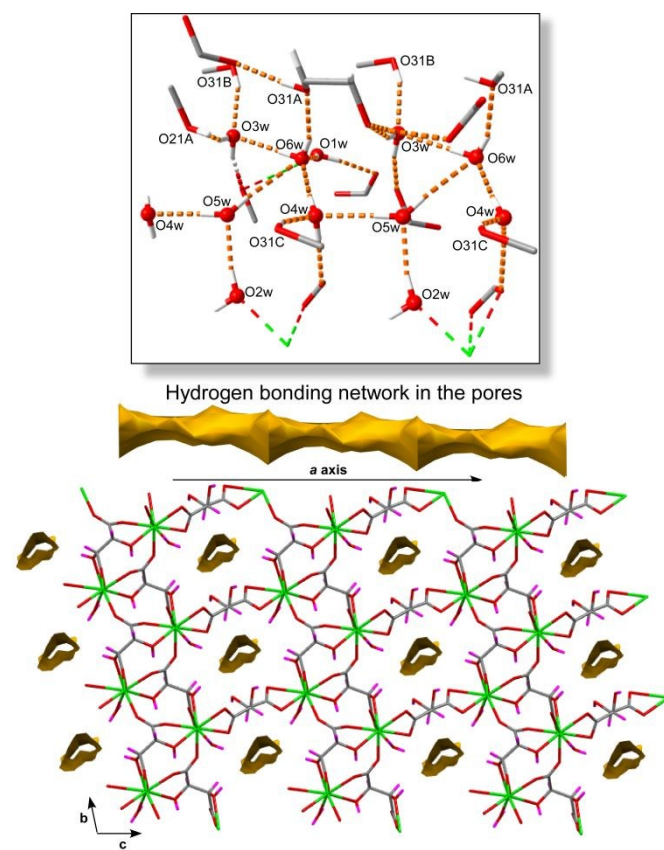
Figure 2. Packing of the 3D framework of **Dy-L** MOF showing the voids and the hydrogen bonding network (including donor atoms names) of the lattice water molecules enclosed in within.

On another level, it must be mentioned that, as expected from the enantiomeric nature of these compounds, D-tartrate based MOFs show an equivalent arrangement which results from the application of an inversion center (see Figure S2 in ESI).

Thermal evolution of the MOFs

The thermal behavior of these MOFs entails an interesting feature because it involves several phase transitions accompanying the dehydration of the crystal structure which may be relevant for their properties. Considering that all compounds show a very similar temperature dependent behavior (see Figures S4-S8 in ESI),

ARTICLE

compound **Tb-L** was selected as a representative sample to conduct a thermodiffractometric study in order to follow plausible structural changes derived from sample heating. Starting from room temperature, the TG curve of the compound describes a small plateau up to 70 °C, which brings no remarkable change in the PXRD data but for a very slight expansion of the unit cell (which increases 1% in volume). Heating the **Tb-L** phase above 90 °C causes shifts in most diffraction maxima (Figure 3) derived from a large shortening of the crystallographic c parameter (Table 1, see also Figures S19–21), compatible with a crushing of the microchannels upon dehydration, and accompanied by a significant cell volume drop (from 556 to 485 Å^3). This plausible loss of water molecules from the pores of this thermally activated phase (**Tb-L'** hereafter) was confirmed by single crystal X-ray diffraction of a single crystal of **Tb-L'**, obtained upon heating a single crystal of the **Tb-L** phase in the diffractometer at 110 °C and cooled down again to 100 K (to improve data collection quality, see Experimental Section). The latter, revealed not only the loss of three water molecules from the channels to yield **Tb-L'**, a compound of $\{[Tb_2(\mu_4\text{-tar})_2(\mu\text{-tar})(H_2O)]\cdot H_2O\}_n$ formula, but also that such dehydration provokes a subtle rearrangement of A tartrate ligands that force the loss of one coordination water molecule of Tb1 too.

The latter tartrate ligand passes from the carboxylate mediated and symmetric $\mu\text{-}\kappa^2O,O':\kappa^2O'',O'''$ bridge to an asymmetric $\mu\text{-}\kappa^3O,O',O'':\kappa^2O''',O''''$ mode in which carboxylate and hydroxyl oxygen atoms take part in the chelating moieties, respectively, for the coordination to Tb1 and Tb2 atoms (Figure 4). Consequently, Tb2 atom moves to a $(O_{carb})_5(O_{hid})_3(O_w)_1$ environment in which one of the originally coordinated carboxylate oxygen atoms (O42A) is now replaced by the hydroxyl O31A atom, in such a way that the CSAPR gets more idealized (S_{CSAPR} passes from 1.159 in **Tb-L** to 0.973 in **Tb-L'**). On its part, $Tb1(O_{carb})_6(O_{hid})_3$ chromophore is best described as a CSAPR once the coordination water molecule is lost. Such a reorganization of the tartrate A ligand brings a remarkable shortening of the Tb···Tb bridge (from 9.13 to 6.66 Å) and the crystallographic c parameter. In any case, this transformation brings no change in the framework topology, since Ln(III) atoms' connectivity is preserved. On another level, the crystallization water molecule remaining in the isolated pores is reoriented so as to get anchored to the framework through strong hydrogen bonding interactions, a fact that allows the resulting framework to maintain some potential porosity (5.4% of the unit cell volume).

Figure 3. Analysis of the thermal behavior of compound **Tb-L**. Note: diffractograms shown in black correspond to temperatures at which phase transition takes place.
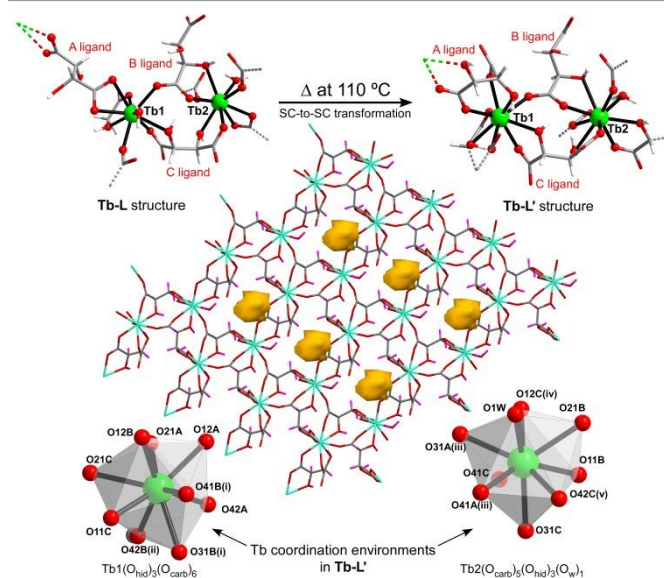
Table 1. Unit cell parameters of the room and high temperature crystalline phases of compound **Tb-L**.[a]

Phase	a	b	c	α	β	γ	V
Tb-L	5.99	7.44	13.28	102.88	101.53	90.95	556
Tb-L'	5.92	7.41	11.97	107.83	103.32	89.94	485
Tb-L''	5.87	7.40	11.91	72.21	76.32	90.15	477
Tb-L'''	5.85	7.49	11.19	79.53	84.22	90.51	479

[a] Unit cell parameters correspond to fitting PXRD data. a, b, and c, α, β and γ, and V, are given in Å, degrees and Å^3, respectively.
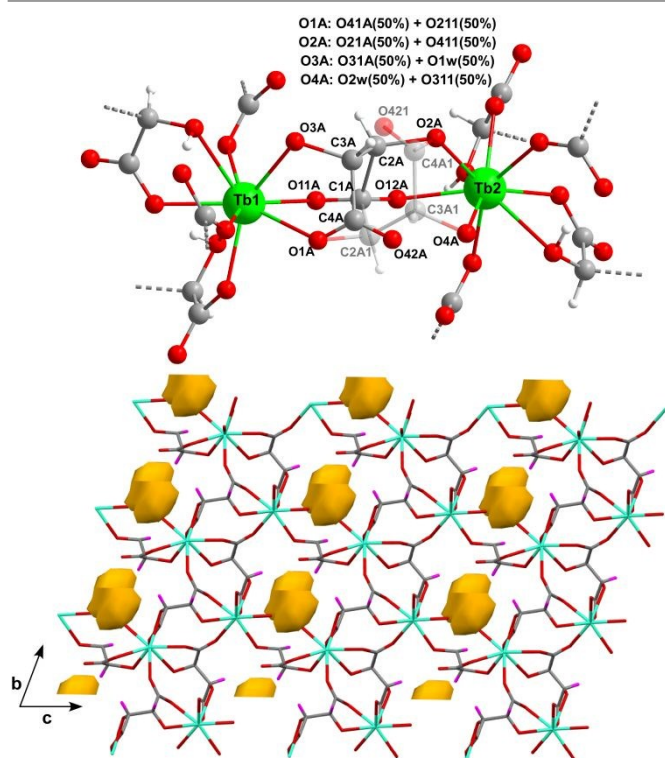

Figure 4. 3D framework of **Tb-L'** displaying the isolated voids. Evolution of the coordination mode of A ligand according to the first dehydration-induced solid state transformation is shown in the upper part. Tb polyhedra of **Tb-L'** are shown in the lower part.

ARTICLE

This first dehydration process is completed at ca. 120 °C and the obtained **Tb-L'** phase is thermally stable up to 150 °C, as derived from the plateau in the TG curve (Figure 3). Interestingly, above 150 °C **Tb-L'** undergoes a new phase transition associated with the loss of a lattice water molecule as confirmed by SCXR data collection on a single crystal of **Tb-L** heated at 200 °C. This new thermally activated phase consists of a compound of {[Tb$_2$(μ_4-tar)$_2$(μ-tar)(H$_2$O)]}$_n$ formula (**Tb-L''** hereafter), where the loss of the lattice water molecule promotes a subtle compression of the flexible framework, as derived from the narrowed α and β angles of the unit cell (see Table 1). Such transformations bring no changes in the connectivity of the framework, or its porosity (the geometrical porosity remains at 5.5% of the actual unit cell volume, Figure 5). Despite this latter fact, tartrate A ligand, which exhibits the μ-$\kappa^3O,O',O'':\kappa^2O''',O''''$ mode by joining to Tb1 and Tb2 atoms, is found to be disordered into two equivalent dispositions (each of which is refined with 50% of occupation) that involve the alternation of different oxygen atoms (carboxylate/hydroxyl and carboxylate/water) occupying two positions of the O$_9$ donor set.

Figure 5. Top: Detail of the disordered tartrate A ligand in the coordination to terbium(III) atoms in **Tb-L''**. Bottom: 3D framework of **Tb-L''** showing the isolated voids.

At this point, it is worth mentioning that the calculated PXRD diffractogram for **Tb-L''** fits well with those acquired in the 150–170 °C but it differs from those taken at the 210–290 °C range. Taking

into account this fact and that the mass loss finishes at ca. 200 °C according to the TG curve, we can assume that this last crystalline phase (stable in the 210–290 °C range) corresponds to the anhydrous [Tb$_2$(tar)$_3$]$_n$ (**Tb-L'''**) product, whose structure could not be determined due to the instability of single crystals at temperatures higher than 200 °C. The PXRD data acquired at 230 °C revealed that **Tb-L'''** phase´s pattern fits well with a triclinic cell that is closely related to that of **Tb-L''** phase, thus suggesting the occurrence of a dense framework with no porosity in **Tb-L'''**. Finally, above 290 °C, two main exothermic processes provoke the decomposition of tartrate ligands into the final Tb$_2$O$_3$ residue.

On another level, the reversibility of the process could be confirmed by PXRD (Figure S22). Following the activation of a sample of **Tb-L** at 210 °C, it was found that **Tb-L'''** phase is transformed back to **Tb-L'** phase after some hours from the thermal activation. In this sequence, **Tb-L''** is not identified during the spontaneous rehydration (probably because it is less stable at standard conditions) although it should be formed in between. Finally, **Tb-L'** remains stable for at least five days until it reverts back to **Tb-L** when exposed to water saturated environments (see ESI for further details).

Static magnetic properties of hydrated phases

The temperature dependent magnetic susceptibility data were measured for polycrystalline samples of L-tartrate based enantiomeric MOFs (compounds **Tb-L** to **Tm-L**) in the 5–300 K range under an applied magnetic field of 1000 Oe. The experimental $\chi_M T$ values at room temperature are close to those expected for the ground states with all Stark levels equally populated.[36] Cooling down the samples cause a progressive drop in the $\chi_M T$ product, as expected for the selective depopulation of the excited Stark sublevels (see S9 section in ESI), although a significant contribution of antiferromagnetic exchange interactions could be also involved given the short ligand mediated Ln⋯Ln pathways present in the structure.[37] The χ_M^{-1} vs. T curves for these compounds followed the Curie–Weiss law almost in the whole temperature range, finding only small deviations for **Ho-L** and **Er-L** below 30 K (see Figure S24 in ESI). Given that there is no available expression to determine the magnetic susceptibilies of 3D systems with large anisotropy, $\chi_M T$ vs. T curves were fitted in the high temperature range (50–300 K) with expressions (Eq. 1, 2 and 3, see ESI) that assume only a splitting of the m_j energy levels ($H = \Delta Jz^2$) in an axial crystal field (Table 2).[38]

Table 2. Best least-squares fits of the experimental magnetic data.[a]

Compound	g	Δ (cm^{-1})
Tb-L	1.44	0.15
Dy-L	1.32	0.31

ARTICLE

Ho-L	1.25	0.28
Er-L	1.23	0.49
Tm-L	1.15	0.53

[a] g is the gyromagnetic factor and Δ is the zero-field splitting parameter.

Inclusion of a zJ' parameter based on the molecular field approximation to account for the magnetic interaction between Ln(III) ions did not improve the fitting and brought almost negligible values (*ca.* −0.01 cm⁻¹). Additionally, DFT calculations were conducted on suitable gadolinium based dimeric models (which possess a spin-only $^8S_{7/2}$ ground state that allow a quantitative analysis of magnetic interactions)[39] to consider all the possible superexchange pathways: (i) Gd1···Gd2 through the carboxylate *syn-anti* and double chelating tartrate double bridge; (ii) Gd1···Gd1 through the double carboxylate chelating ligand; (iii) Gd1···Gd2 through the chelating-monodentate tartrate ligand. These calculations support the existence of negligible exchange interactions of ferromagnetic nature ($J \approx 0.003$ cm⁻¹, see Figure S25 in ESI), meaning that the 3D framework can be considered as an interconnected network of isolated Ln(III) centers from a magnetic point of view.

Dynamic magnetic properties of hydrated and dehydrated phases

As inferred from the crystal structure description (see CShMs in Table S11–13), the ligand field appears to be quite distorted and not especially suitable to stabilize high m_J ground states either for oblate or prolate ions. However, sample dehydration may tune the magnetic properties of these dehydrated phases derived from the reorganization of particularly the first but also the second coordination sphere of the metal. Due to the aforementioned distorted crystal field, only the most promising analogues (**Tb-L**, **Dy-L** and **Er-L**) were studied. Alternating current (*ac*) magnetic measurements revealed a lack of χ''_M signals under zero applied *dc* field (Figures S26–28 in ESI) for all compounds. This could be attributed to the existence of quantum tunneling of the magnetization (QTM) and to the relatively short Ln···Ln distances (ca. 5.8 Å), which could provoke weak dipolar interactions that facilitate the fast relaxation of the magnetization hiding the SMM behavior.[40] It is well known that this effect might be partially or totally quenched by applying an external magnetic field (H_{dc}), and accordingly, under an H_{dc} = 1 kOe the three compounds show non-zero χ''_M signals. **Tb-L** displays maxima at the highest frequencies (υ), whereas at lower frequencies only a small shoulder can be identified, confirming that QTM is still operating (Figure 6a). In the case of **Dy-L**, a small maximum could be identified only at the highest frequency and at the temperature limit of the device, suggesting a very small energy barrier for the reversal of the magnetization (Figure 6b). In contrast, **Er-L** shows quite well-

defined maxima below 4 K although QTM is shown to be still operative (Figure 6c). For **Tb-L** and **Er-L** the temperature dependence at each frequency was fitted to the generalized Debye model obtaining relaxation times for each temperature (Figures S30 and S34 in ESI). The noisy signals of the former allow to a poor fit of the data (inferred by the shape of χ''_M vs T curves), the high α values (around 0.5) obtained from the Cole-Cole plots suggest the presence of simultaneous relaxation processes. However, a reliable linear fit to the Orbach process affords an effective energy barrier of U_{eff} = 6.5 K and a pre-exponential factor τ_0 = 2.04·10⁻⁶ s (Figure 6a). The presence of SMM behavior in the Tb(III) analogue is worth mentioning. Actually, for non-Kramers ions a rigorous axial symmetry should be maintained in order to have a bi-stable ground state,[41] and this is not the case. In fact, apart from the CShMs measurements, the thermal evolution of the $\chi_M T$ product is indicative of a relatively weak crystal field effects. Compounds with a well-defined axial ligand field usually display characteristic profiles where a very smooth decrease is observed in the whole temperature range with a sudden abrupt decrease at the lowest temperature (exhibiting magnetic blocking).[15,42] However, the presence of field induced SMM behavior is not novel for low symmetry systems, as in compound **Tb-L** (see Table S11 in ESI). In fact, this kind of systems can show quasi-degenerate ground states and consequently display slow relaxation of the magnetization.[43] In the case of **Er-L**, at the lowest temperatures, nearly temperature independent relaxation times were obtained (indicative of QTM), whereas at the highest temperatures the linear portion suggests the presence of the Orbach process. This is in good agreement with the high α values (0.49 at 2.0 K and 0.42 at 3.3 K) achieved from the Cole-Cole plots. Hence, the relaxation times were fitted to the simultaneous presence of Orbach and QTM processes (Equation 1) with the following set of parameters: U_{eff} = 33.8 K, τ_0 = 6.45·10⁻¹⁰ s and τ_{QTM} = 6.54·10⁻⁴ s. The dashed lines (Figure 6c, inset) indicate the contribution of each process at different temperatures.

$$\tau^{-1} = \tau_{QTM}^{-1} + \tau_0^{-1}exp(-U_{eff}/k_BT) \ (Eq. \ 1)$$

ARTICLE
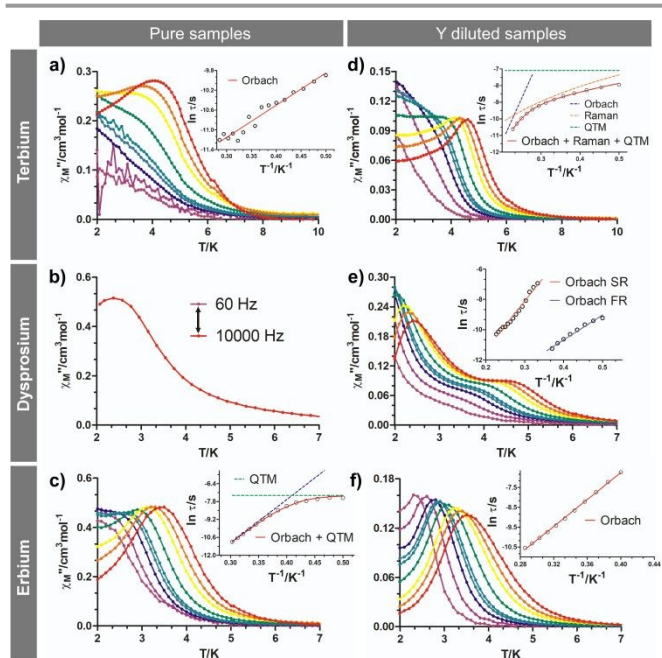
Figure 6. Temperature dependence of the out-of-phase ac susceptibility under H_{dc} = 1 kOe for the pure **a) Tb-L**, **b) Dy-L** and **c) Er-L** samples and diluted **d) TbY-L**, **e) DyY-L** and **f) ErY-L** samples. Insets: Temperature dependence for the relaxation times and the best fits of the data to different relaxation processes.

In view of the residual unquenched QTM occurring in the pure samples, the magnetic properties of equivalent but magnetically diluted samples (**TbY-L**, **DyY-L** and **ErY-L** hereafter) were analyzed, in which the contribution of possible weak dipolar interactions is avoided. The diluted samples were prepared by co-crystallizing the diamagnetic Y(III) counterpart along with the paramagnetic ions in a 9:1 Y(III):Ln(III) ratio. Similarly to what occurs with the non-diluted samples, under zero *dc* field no out-of-phase response was detected for **TbY-L** and **ErY-L**. Interestingly, **DyY-L** displays a weak χ''_M signal at low temperature, though no maximum is observed (Figure S37). Once again, the measurements were repeated with H_{dc} =1 kOe and substantial differences were obtained. First of all, the peaks for **TbY-L** are better defined and shifted to higher temperatures (Figure 6d). However, as observed for **Er-L**, the curves of **TbY-L** still display the characteristic tail attributed to QTM below the maxima. Fitting of the χ''_M vs υ to obtain the relaxation times (Figure S40) turned to be more reliable in agreement with the better defined of χ''_M vs T maxima. The relaxation times present the typical curvature suggesting the simultaneous presence of multiple relaxation pathways (Figure 6d, inset), in good agreement with the high α values extracted from the Cole-Cole plots (0.40 at 2.0 K and 0.11 at 4.4 K). The best fitting of the data was achieved with equation 2, which accounts for Orbach, Raman and QTM relaxation processes (Table 3).

$$\tau^{-1} = \tau_{QTM}^{-1} + BT^n + \tau_0^{-1}exp(-U_{eff}/k_BT) \ (Eq. \ 2)$$

The following set of parameters was obtained: U_{eff} = 52.0 K, τ_0 = 3.42·10⁻¹⁰ s, B = 177.9, n = 3.135 and τ_{QTM} = 8.33·10⁻⁴ s. Regarding the n parameter, values between 1 and 6 can be considered reasonable.[44]

The Dy(III) analogue shows typical SMM behavior below 5 K with two sets of out-of-phase peaks in the 2.0-2.5 K and 3.5-4.5 K temperature ranges, attributed to fast (FR) and slow relaxation (SR), respectively (Figure 6e). In spite of the fact that they are clearly identified in the χ''_M vs T plot, FR and SR appear to be somehow mixed complicating the analysis. Certainly, the Cole-Cole and χ''_M vs υ plots exhibit slightly mixed semicircles and broad maxima, respectively, despite of which the analysis with a simple Debye model gave quite reasonable results. In any case, in χ''_M vs υ plots (Figure S43) the broad maximum observed at 2.0 K at around 1000 Hz is moved to higher frequencies as the temperature is increased, completely disappearing at 2.6 K. This is attributed to the FR. On the other hand, the maximum at high frequencies (around 10000 Hz) appears again at higher temperatures (4.0 K) but it rapidly disappears (at 4.4 K). The latter one corresponds to the SR, which was hidden by the larger intensity of the FR. This effect may be well illustrated by plotting the relaxation times extracted from the fit (Figure S44). The first low temperature points (2.0-2.8 K) display a quite linear trend that corresponds to the effective energy barrier associated to the FR. As the temperature is increased, the relaxation times become slower as the SR starts contributing, while another linear portion related to the barrier of SR is observed at the highest temperatures (4.0-4.4 K). The occurrence of two relaxation processes demands a fitting with the sum of two modified Debye functions to consider each relaxation independently, which was performed with the CCFIT Software[45] to obtain two sets of relaxation times. Thus, Arrhenius plots constructed for both relaxation processes (see inset of Figure 6e) afford effective energy barriers for the reversal of the magnetization and τ_0 values of 17.7 K with 1.78·10⁻⁸ s and 32.3 K with 1.83·10⁻⁸ s for FR and SR, respectively.

For **ErY-L**, the combination of the external magnetic field along with the dilution process is appropriate to completely quench the fast QTM, given the trend to zero observed for the χ''_M signals below the maxima as well as their well definition for the entire set of frequencies. Accordingly, the fitting of the relaxation times follows a linear trend in the whole temperature range, giving an effective energy barrier of U_{eff} = 33.9 K and τ_0 = 1.52·10⁻⁹ s, which are very similar values to the non-diluted samples.

Table 3. Fitting parameters of the magnetic ac measurements.

Compound	U_{eff} (K)	τ_0 (s)

ARTICLE

Tb-L	6.5	$2.04 \cdot 10^{-6}$
Dy-L	–	–
Er-L[a]	33.8	$6.45 \cdot 10^{-10}$
TbY-L[a]	52.0	$3.42 \cdot 10^{-10}$
DyY-L[b]	17.7 / 32.3	$1.78 \cdot 10^{-8}$ / $1.83 \cdot 10^{-8}$
ErY-L	33.9	$1.52 \cdot 10^{-9}$

[a] These values are estimated from a fitting in which Raman and/or QTM relaxation mechanisms are considered. [b] The two values correspond to FR/SR processes.

The hydrothermal synthesis of these MOFs, based on, allows the coordination of water molecules to the oxophilic Ln(III) ions. As afore mentioned, the dynamic magnetic properties of SMMs are known to be directly correlated to the coordination environment, meaning that changes in the number of relaxation processes or the height of the effective energy barrier may be expected. Hence, we have studied three out of the four existing diluted dysprosium phases (as synthesized **DyY-L** and thermally activated **DyY-L'** and **DyY-L'''**) to analyze how the loss of lattice/coordination water molecules modulate the dynamic magnetic properties of these materials. The Dy-based analogue was chosen due to two main reasons: a) the non-activated (**DyY-L**) phase shows two thermally activated relaxation processes in such a way that more significant differences in the data could be expected and b) the Dy(III) ion is, probably, the most promising Ln(III) ion when designing high performance SMMs.

Under an external zero *dc* field, **DyY-L'** does not show any maximum in the χ''_M vs T plot (Figure S50) as it occurs for **DyY-L**. When applying a magnetic field of 1 kOe, the highest frequency curves (4000-10000 Hz) display well defined maxima in the 2.0-3.0 K range (Figure 7a). Interestingly, the second set of maxima in **DyY-L** associated to the SR process has disappeared for the activated **DyY-L'** analogue, suggesting that the reorganization of the tartrate ligands (which could affect the molecular vibrations and, possibly, the relaxation modes) as well as the loss of the coordinated and lattice water molecules have a considerable impact in the relaxation process. Note that this first dehydration involves a complete rearrangement of one of the Dy(III) centers in **DyY-L'** (Dy1 loses the coordination water molecule) so no direct association can be established between Dy centers and relaxations (FR and SR) for different phases. The Cole-Cole plots of **DyY-L'** suggest a wide distribution of relaxation mechanisms, showing α values in the range of 0.31-0.52 (for 2.0 and 3.0 K, respectively). Thus, the relaxation times were fitted using equation 1 giving the following set of parameters: U_{eff} = 16.7 K, τ_0 = $6.87 \cdot 10^{-8}$ s and τ_{QTM} = $1.91 \cdot 10^{-4}$ s.
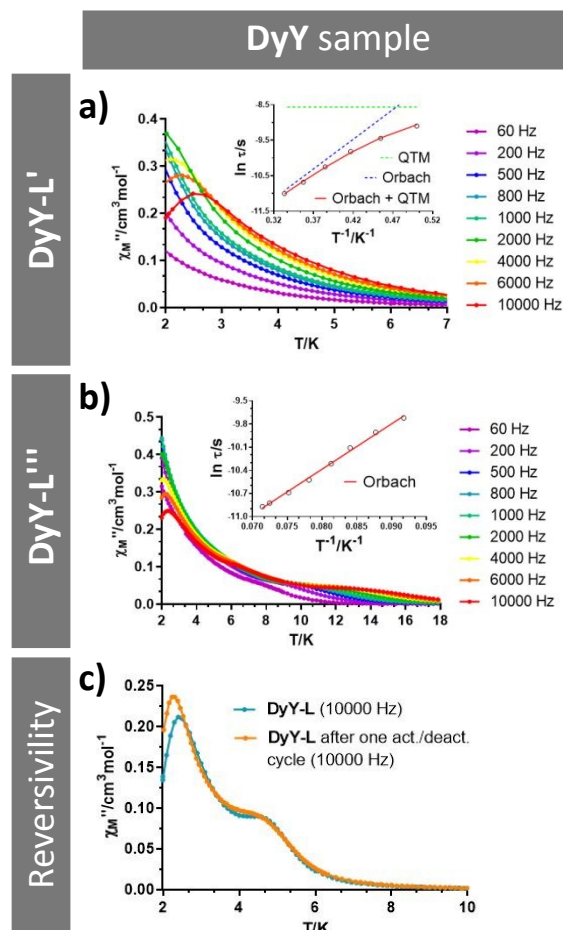
Figure 7. Temperature dependence of the out-of-phase *ac* susceptibility under an external magnetic field of 1 kOe for **a) DyY-L'** and **b) DyY-L'''** samples. Insets: temperature dependence for the relaxation times and best fits. **c)** *ac* curves at 10000 Hz for the non-activated and fully dehydrated/rehydrated sample.

In order to focus on the most interesting switch of the magnetic properties through the thermal activation of the material, the completely dehydrated **DyY-L'''** phase was studied (see S1 section in the ESI for further details on sample preparation). Even though SCXR structure could not be solved for this compound, TDX and TG analysis confirm the absence of water molecules in the framework of **DyY-L'''** (see Figure 3), meaning that a new rearrangement of the ligand field must have occurred, which could promote a second switch in the magnetic relaxation behavior. Indeed, *ac* measurements on **DyY-L'''** under H_{dc} =1 kOe (no maxima were observed under zero *dc* field, see Figure S54) display a non-defined but clearly appreciable new set of maxima at temperatures as high as 13 K (Figure 7b). This increase in the temperature may be originated from a new and more axially defined crystal field around Dy(III) ions, which would provoke a bigger splitting between the ground and excited states that in turn increases the value of the

ARTICLE

effective energy barrier. However, the facts related to the molecular vibrations of the lost coordination water molecule or even the subsequent reorganization of the phonon-structure of the material cannot be discarded. The data was then analyzed in the 10.9-14 K temperature range, obtaining α values indicative of a quite wide distribution of relaxation processes (0.35 at 10.9 K and 0.30 at 14.0 K, Figure S57) although relaxation times extracted from the χ''_M vs υ curves describe a linear Arrhenius plot (Figure 7b, inset). This incoherence might be due to the small shoulder below the analyzed temperature (in the 6–8 K range), accordingly assuming that another relaxation process, responsible of enlarging the α value when lowering the temperature, is taking part. However, the tendency clearly indicates that the relaxation distribution is becoming narrower and therefore the data was fitted to a pure Orbach process with an effective energy barrier of U_{eff} = 58.7 K and τ_0 = 2.82·10^{-7} s.

Finally, the reversibility of the magnetic properties was also studied by collecting a new *ac* curve at 10000 Hz on a sample after one entire activation/deactivation cycle. As depicted in Figure 7c, both *ac* curves at 10000 Hz almost overlap, confirming the reversible character of the material, in good agreement with the PXRD analysis conducted.

Luminescence properties of hydrated phases

Lanthanide centered emissions in coordination polymers (CPs) are known to be useful for developing solid-state photodevices[46] given their intense emissions in the visible spectra or in the near-infrared (NIR) region[47]. For this reason, photoluminescence measurements were carried out on polycrystalline samples of all L-enantiomeric compounds (**Tb-L** to **Tm-L**) given that the measured luminescent properties are enantiomer independent, as observed for the **Dy-L** and **Dy-D** pair (Figure S58 in ESI). Whereas compounds **Ho-L** and **Er-L** exposure to UV excitation yielded no characteristic Ho(III) and Er(III) based emissions these compounds provided an almost identical band in the 400–650 nm range (see Figures S59–60) attributable to the n ← π* emissions of the metal coordinated tartrate ligands. With regard to those compounds containing Ln(III) atoms potentially emitting in the visible range, non-radiative relaxation tends to be less important since, being more energetic than NIR emissions, it is comparatively less quenched by molecular vibrations, i.e. thermal deactivation.[17] Taking into account that these emissions arise from ligand-to-metal charge transfers (LMCT), and that they may change according to the temperature, the latter parameter was also studied. Such a LMCT in Ln(III)-organic systems is known to proceed from the first excited triplet state (T_1), so we made use of DFT calculations to estimate the energy and shape of that state. In T_1, the MO shows the lobes spread over the whole molecule but especially over the oxygen atoms (Figure S73). Moreover, the calculation to estimate the vertical excitation energy

between T_1 and the ground singlet state (S_0) with the same optimized geometry, which presents an almost identical shape of T_1, gives a value of 19639 cm^{-1} which can be considered as the energy of T_1. No Tm(III) based emissions were observed for compound **Tm-L**, which showed a similar spectrum to **Ho-L** and **Er-L**. When compounds **Tb-L** and **Dy-L** are excited at room temperature under monochromatic 325 nm light, they present emission spectra composed of a minor wide band assigned to the ligand fluorescence (as it peaks at ca. 400 nm and resembles the emission shown by compounds **Ho-L** and **Er-L**) in addition to intraionic transitions associated with Ln(III) ions (Figure 8).
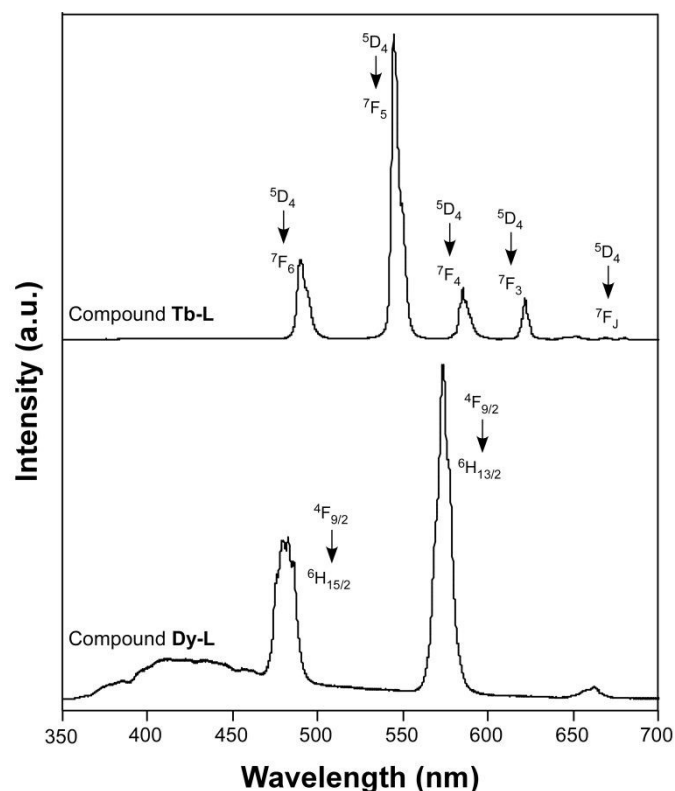
Figure 8. Emission spectra of compounds **Tb-L** and **Dy-L** recorded at room temperature under laser λ_{ex} = 325 nm.

In particular, compound **Tb-L** displays four main groups of signals sited at 490 nm ($^7F_6$ ← $^5D_4$), 544 nm ($^7F_5$ ← $^5D_4$), 585 nm ($^7F_4$ ← $^5D_4$) and 622 nm ($^7F_3$ ← $^5D_4$) arising from intraionic transitions of Tb(III) ions. A comparatively weaker luminescence is observed for the **Dy-L**, since in addition to the characteristic multiplets centered at 481 nm ($^6H_{15/2}$ ← $^4F_{9/2}$), 573 nm ($^6H_{13/2}$ ← $^4F_{9/2}$) and at 662 nm ($^6H_{11/2}$ ← $^4F_{9/2}$), the band assigned to tartrate ligand fluorescence (previously shown for **Ho-L** and **Er-L**) is significantly stronger. It is worth noticing the large intensity of the second band, which dominates the spectrum, and the fact that the third band is observed,

ARTICLE

conversely to most of reported lanthanide-organic complexes but habitually present on strongly emitting inorganic phosphors.[48] Indeed, these strong emissions are quite surprising considering that the tartrate ligand lacks strong absorbing chromophores. An inspection of the excitation spectra at the main line (λ_{em} = 544 for **Tb-L** and 573 nm for **Dy-L**) reveals the absence of any significant wide band in the spectra, thus indicating the lack of any ligand centered excitation. Instead, only narrow bands associated with the intraionic f-f transitions of the lanthanide are present, among which $^7F_6 \rightarrow {}^5L_9$ and $^6H_{15/2} \rightarrow {}^5P_{3/2}$,[49] one of the most intense bands respectively for **Tb-L** and **Dy-L** samples, fall within the employed excitation wavelength (λ_{ex} = 325 nm). The obtained results are in agreement with the micro-PL images taken on a microscope in which some selected excitation lines (λ_{ex} = 365, 435 and 536 nm) have been chosen. Under UV excitation, **Tb-L** displays intense green emission according to the fact that the excitation band corresponding to the $^5D_4 \rightarrow {}^6L_{10}$ (at 364 nm) fits well with λ_{ex} = 365 nm. On the other hand, **Dy-L** sample is not such effectively excited through any intraionic transition (see ESI).

The overall low energy transfer observed from tartrate ligands to Ln(III) centers may be explained according to the lower energy of T_1 state (calculated at $\approx$ 19639 cm^{-1} through DFT methodology) than those emitting levels of Ln(III) atoms ($^5D_4$ level for Tb(III) $\approx$ 20500 cm^{-1}, and $^4F_{9/2}$ level for Dy(III) $\approx$ 20800 cm^{-1}).[50] According to Latva's empirical rule,[51] the optimal ligand-to-metal energy transfer process for Ln(III) based complexes needs an energy gap in the 2500–4000 cm^{-1} range, which is surpassed in all cases. This rule also explains why Tm(III) atoms (with the emitting $^1G_4$ level at ca. 21600 cm^{-1}) do not show the characteristic emission in compound **Tm-L**.

To get deeper insights, the luminescence properties of **Tb-L** and **Dy-L** were measured at 10 K to avoid the vibrational quenching derived from the thermal energy of the bond electrons.[52] Upon laser excitation (λ_{exc} = 325 nm), emission spectra of samples revealed a significant enhancement of the emitted light, which allowed distinguishing many of the individual transitions grouped in each manifold (Figure S66).[53] It must be noted that the enhancement comes from the increased efficient intraionic excitation and not from an improved antenna effect given the similar shape of the low temperature excitation spectra (see ESI). A common feature to all spectra is the occurrence of ligand-based fluorescence, though the intensity of these bands is comparatively low with those recorded at room temperature. In the spectrum of the Tb(III) compound (**Tb-L**) seven multiplets corresponding to the ^7F_J (J = 0–6) $\leftarrow {}^5D_4$ transitions are observed, although the last three multiplets are relatively weak. Given the good emission capacity of the Tb-based compound, a detailed analysis of its emission was performed as a function of the temperature (measuring a spectra each 25 °C). As inferred from Figure S67 (see ESI), the emission capacity in terms of integrated emission from room temperature to 10 K remains almost

unchanged (covering the 350–700 nm range). On the other hand, the spectrum of **Dy-L** displays the same three bands centered at 483, 578 and 664 nm, among which the second one (green emission) also exhibits the highest intensity. Nonetheless, it must be remarked that there is a change in the relative intensity of the bands with the temperature, passing from an intensity ratio of 2.13 to 1.4. The analysis of the emission lifetimes revealed monoexponential decays from both compounds in good agreement with the fact that although the crystal structure contains two independent Ln(III) centers, they have identical coordination shells which makes them equivalent from the spectroscopic viewpoint. The fitting of the curves with the exponential function [$I_t = A_0 + A_1 \cdot \exp(-t/\tau)$], gives a relatively large lifetime of ca. 1 ms, which is completely stable with the temperature. This fact supports, once again, that decreasing the temperature brings no enhancement of the radiative part but it only implies a decrease of the non-radiative losses which translate in an overall improvement of the emission capacity. The fitting of the decay curve for **Dy-L** gives homogenous lifetimes for the two main emission maxima, with a value of ca. 30 μs. On its part, the low temperature also decreases the non-radiative quenching in **Tm-L** up to the point that thulium(III) centered emissions can be traced in the emission spectrum recorded at 10 K (Figure S61).

With the aim of getting deeper insights into the enhancement of the PL signal at low temperature, the DFT calculation to estimate the energy of the T_1 state is conducted by fixing 10 K as the temperature. The T_1–S_0 gap for the tartrate molecule at triplet geometry enlarges up to 23398 cm^{-1}, meaning that the energy gap regarding lanthanide's excited emissive levels could fit into the efficient region considered by Latva and that the more brilliant emissions of **Tb-L** and **Dy-L** (in addition to the Tm-based emission per se) are due to not only the lower vibrational quenching but also to a more efficient ligand-to-lanthanide energy transfer.

Luminescence properties of dehydrated phases

Considering the exciting transformations taking place when heating the synthesized samples, as shown before in the "Thermal evolution of the MOFs" section, we decided to explore the modulation of the PL signal with the loss of lattice/coordination water molecules, and we selected **Dy-L** as an example. The emission spectrum recorded for **Dy-L′** at RT (thermally activated at 110 °C) displays a clear increase of the absolute emission (21 times) mainly due to the tartrate-centered fluorescence band, which gets of similar intensity compared to the Dy-based signals (see Figures S68–70 in the ESI for further details). This impressive rise may be attributed to the loss of O–H oscillators of water molecules in the coordination and outer spheres, which are known to act as efficient quenchers of the luminescence.[54] The second and third transformations that render **Dy-L″** and **Dy-L‴** phases when heating

ARTICLE

the sample at 190 and 210 °C, respectively, exhibit an almost immediate rehydration back to **Dy-L'**, so their luminescent properties had to be performed directly under vacuum to ensure that rehydration is prevented. **Dy-L''** and **Dy-L'''** phases exhibit an almost indistinguishable spectrum, dominated by the Dy-centered bands (peaking at λ_{ex} = 482 and 573 nm). The RT spectra collected for **Dy-L'** and **Dy-L'''** phases (after heating them under vacuum to 110 and 210 °C, respectively) are easily distinguished by the position and relative intensity of the tartrate-centered fluorescence band, which is dropped redshift from λ_{em} = 407 nm for **Dy-L'** to 517 nm for **Dy-L'''**. All these modifications in the PL, though not too dramatic, could be enough as to employ these MOFs for sensing utilities.

Circular dichroism (CD) experiments on hydrated phases

The chiral character of the prepared MOFs prompted us to explore their differential absorption properties of circularly polarized light. CD (and the corresponding UV-Vis) spectra were acquired for water suspensions of each pair of enantiomeric MOFs, as well as for the water solutions of L- and D- tartaric acid samples. As observed in Figure 9, CD spectra of the MOFs are characterized by two well-defined regions: an intense band centered at 195 nm and a less intense one at 221 nm, with opposite Cotton effects, respectively. Bands at the same wavelengths are of course present in the corresponding UV-Vis spectra and can be assigned to n → π* transitions according to TD-DFT calculations (see ESI). CD spectra of enantiomeric samples are mirror images, clearly indicating the enantiopurity of the samples. These results are in agreement with those reported by Tushari et al. for compounds **Er-L** and **Er-D**.[55] Crucially, CD spectra of water solutions of L- and D-tartaric acids (free ligands) show two bands at 190 and 214 nm which are blue-shifted and inverted (+/- sign) compared to the ones observed for the MOFs samples.
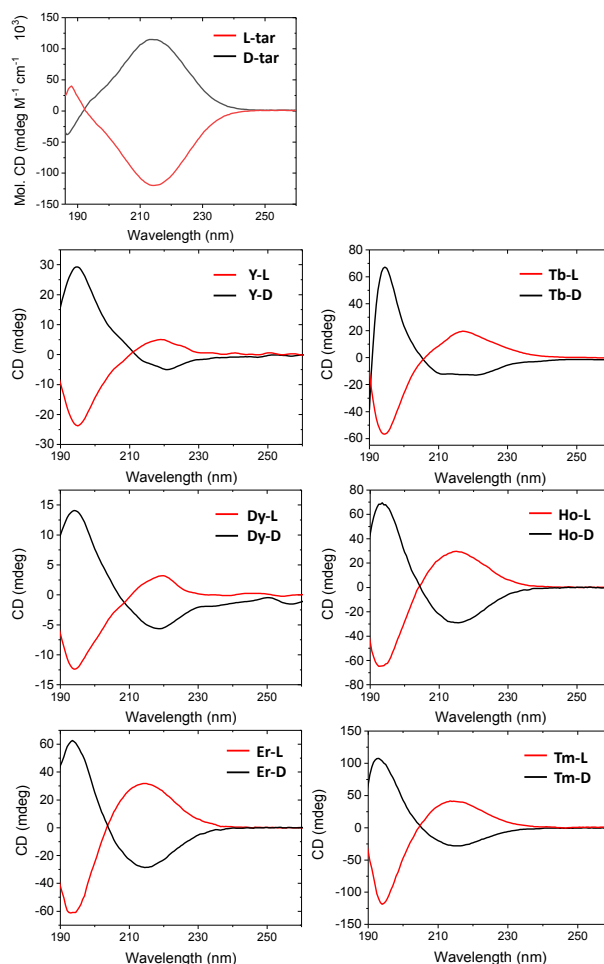

Figure 9. CD spectra recorded for all compounds.

Circularly polarized luminescence (CPL) experiments

CPL is a well-known property of lanthanide cations.[56] It comes from magnetic dipole allowed Ln centered *f-f* transitions, usually showing a large degree of circular polarization.[57] In this work, we were able to measure the circularly polarized emission of the Tb-based MOF, resulting, as far as we are aware, in the second example of this chiroptical property in chiral MOF.[28] The CPL spectra centered at the $^7F_5 \leftarrow {}^5D_4$ transition of Tb compounds are plotted in Figure 10. In a chiral environment, the degeneration of the sublevels of the band disappears, showing a complex pattern. The complexity derives from the different signs and magnitudes of the rotational strengths of the transitions, a fact that has been extensively reported.[58] In this particular, the spectra reveal the presence of two main bands (centered at 540 and 555 nm) while a third band sited at 560 nm may be also guessed. Interestingly, the two main CPL bands show symmetrically opposed signs with

ARTICLE

luminescence dissymmetry factor g_{lums} values around 4 10^{-3} and 1 10^{-3}, respectively. This fact precludes the presence of any artefact in our measurements (see also ESI). These values are also in agreement with other previously reported data of chiral Tb CPs.[59] Although we could detect the emission of other fluorescent bands with low intensity, their weak chiroptical response avoided to extract reliable data for such bands. CPL experiments run on the rest of the samples did not yield measurable CPL signals.
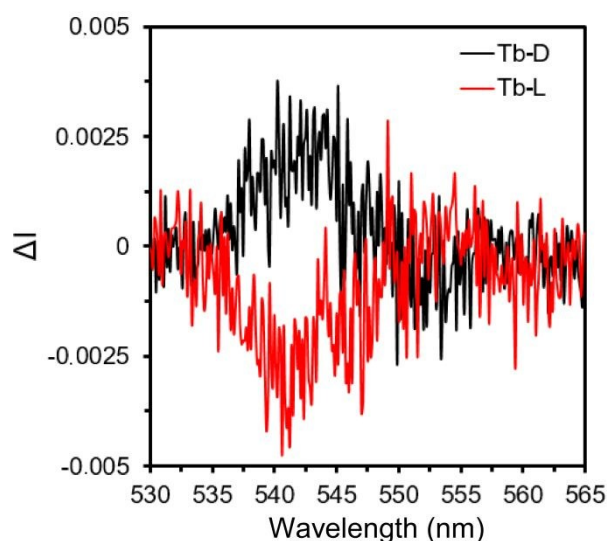

Figure 10. CPL spectra for the $^7F_5 \leftarrow {}^5D_4$ transition for **Tb-L** and **Tb-D** compounds.

Conclusions

A family of five pairs of isostructural and enantiomerically pure MOFs have been synthesized, based on Ln(III) cations and either L- or D- tartrate ligands. The compounds consist of 3D open frameworks built up from the junction of nine-coordinated Ln(III) atoms and chiral (L- or D-) tartrate ligands which leave narrow microchannels that are filled by lattice water molecules to obey ${[Ln_2(\mu_4\text{-tar})_2(\mu\text{-tar})(H_2O)_2]\cdot xH_2O}_n$ formula. The framework is somewhat flexible as to admit a variable number of lattice water molecules as well as significant rearrangements of the Ln(III) centers according to not only the ion size (drop of the coordination number with Tm counterpart) but also to the increase of the temperature. In fact, several thermally-activated phases that present partially (**Ln-L'** and **Ln-L''**) or completely (**Ln-L'''**) dehydrated crystal structures, some of which have been isolated and their magnetic and luminescence properties characterized.

As-synthesized Dy, Tb and Er based MOFs exhibit field-induced single-molecule magnet behavior with moderate barriers for the reversal of the magnetization (U_{eff}) due to a residual unquenched quantum tunneling (QTM) occurring, particularly for the Dy

counterpart. When the materials are magnetically diluted in a Y-based matrix, QTM is suppressed bringing an enhancement of the ac signal and an increase of the U_{eff}, mainly for the case of the DyY material which in turn exhibits a less frequent dual dynamics composed of fast (FR) and slow (SR) relaxations. Thermal activation on **DyY-L** effectively modulates the magnetic response of the material on the basis of the progressive loss of coordination water molecules and subsequent rearrangement of tartrate ligands around the Ln-centers. The drop of one water molecule in **DyY-L'** limits the SMM behavior to a unique FR and drops U_{eff} (from 17.7 / 32.3 K for **DyY-L** to 16.7 K for **DyY-L'**) whereas U_{eff} rises up to 58.7 K in the completely anhydrous structure of **DyY-L'''**.

Tartrate ligands are able to sensitize Tb and Dy centers in these materials rendering quite strong characteristic intraionic emissions. The absence of significant emissions for the Ho and Er near-infrared (NIR) emitters derives from the poor overlap between the tartrate's triplet state and the Ln emitting levels, in good agreement with the DFT calculations performed. Measuring the spectra at low temperature (10 K) brings stronger emission capacity due to decrease of the non-radiative losses. A similar effect is observed for the thermally activated **Dy-L'** phase in agreement with the lower amount of coordination water molecules. Further dehydration of the MOF under controlled conditions (to prevent spontaneous rehydration of **Dy-L''** and **Dy-L'''**) brings some slight changes in the PL emission, mainly based on a significant shift of 110 nm for the tartrate-centered fluorescence band.

The slight changes observed in both the magnetic barrier and the emission spectra of the Dy-based material according to its reversible dehydration/rehydration opens the way to the potential use of this system as humidity sensor. Moreover, interesting CPL emission, which is practically unexplored in MOFs, is observed for the Tb-based compounds with $|g_{lum}|$ values of up to 4 10^{-3}. The observed response, yet moderate, paves the way to promising analytical/sensing applications in the future.

Experimental Section

Synthesis of ${[Ln_2(\mu_2\text{-tar})_2(\mu\text{-tar})(H_2O)_2]\cdot xH_2O}_n$ [where Ln(III) = Tb, Dy, Ho, Er and Tm]

Single crystals of all compounds were obtained through a previously reported[60] hydrothermal procedure. Briefly, 5 mL of an aqueous solution containing 0.6 mmol of the corresponding Ln(III) nitrate were mixed with 5 mL of an aqueous solution of the chiral tartaric acid (L- or D-H$_2$tar) (135.1 mg, 0.9 mmol) in 5 mL and sonicated. The resulting solution was heated in a Teflon liner at 140 °C for 48 h and slowly cooled down to room temperature. Elemental analyses (EA) and further details on the synthesis can be found in the ESI.

ARTICLE

Physical Measurements

Details on the methods and equipment used for the characterization by means of EA, metal content, FT-infrared spectra, thermal analyses (TG/DTA), and magnetic susceptibility measurements can be found in S1 section of the ESI.

X-ray Diffraction Data Collection and Structure Determination

X-ray data collections and reductions were acquired on suitable single crystals of **Ln-L/D** and activated **Tb-L'** and **Tb-L''** with Agilent Technologies Super-Nova and Bruker VENTURE diffractometers, using WINGX crystallographic package[61] to refine the crystal structures (see section S2 and Tables S1–2 of the ESI for further details). The supplementary crystallographic data have been deposited with the Cambridge Crystallographic Data Center (CCDC numbers 1981571-1981583). Details of X-ray powder diffraction (PXRD) patterns and variable-temperature PXRD acquisition are also gathered in S2 section of the ESI.

Photophysical and chiroptical properties

Fluorescence excitation and emission spectra were recorded on a Varian Cary-Eclipse Fluorescence Spectrofluorimeter (at RT) and Edinburgh Instruments FLS920 spectrometer (10 K), whereas an Olympus optical microscope was employed acquire the photographs (see S3 section in ESI). CD spectra on a Jasco J-815 or on an Olis DSM172 equipped with a Hamamatsu 150 W xenon arc lamp as light source. Circularly polarized luminescence (CPL) measurements were performed on an Olis DSM172 spectrophotometer (see S4 section in the ESI).

Computational details

DFT optimization, TD-DFT methodology, and broken-symmetry calculations were conducted with Gaussian 09 package[62] at B3LYP/6-311G++(d,p)[63,64] theory level (see S5 section in the ESI).

Notes and references

1.- (a) V. Guillerm, D. Kim, J.F. Eubank, R. Luebke, X. Liu, K. Adil, M.S. Lah, M. Eddaoudi, *Chem. Soc. Rev.*, 2014, **43**, 6141. (b) M. Eddaoudi, D.F. Sava, J.F. Eubank, K. Adil and V. Guillerm, *Chem. Soc. Rev.*, 2015, **44**, 228. (c) M. O'Keeffe and O. M. Yaghi, *Chem. Rev.*, 2012, **112**, 675. (d) D. J. Tranchemontagne, J. L. Mendoza-Cortés and M. O'Keeffe, *Chem. Soc. Rev.*, 2009, **38**, 1257. (e) S. R. Batten, N. R. Champness, X.-M. Chen, J. Garcia-Martinez, S. Kitagawa, L. Öhrström, M. O'Keeffe, M. P. Suh and J. Reedijk, *Pure* Appl. *Chem.*, 2013, **85**, 1715.

2.- (a) M. D. Allendorf and V. Stavila, *CrystEngComm*, 2015, **17**, 229. (b) Y. B. Zhang, H. L. Zhou, R. B. Lin, C. Zhang, J. B. Lin, J. P. Zhang and X. M. Chen, *Nat. Commun.*, 2012, **3**, 642. (c) J. Cepeda, G. Beobide, O. Castillo, A. Luque and S. Pérez-Yáñez, *Coord. Chem. Rev.*, 2017, **352**, 83.

3.- (a) O. K. Farha, I. Eryazici, N. C. Jeong, B. G. Hauser, C. E. Wilmer, A. A. Sarjeant, R. Q. Snurr, S. T. Nguyen, A. O. Yazaydin and J. T. Hupp, *J. Am. Chem. Soc.*, 2012, **134**, 15016–16021. (b) H.-C. J. Zhou and S. Kitagawa, *Chem. Soc. Rev.*, 2014, **43**, 5415–5418. (c) J.-C. Tan and B. Civalleri, *CrystEngComm*, 2015, **17**, 197–198.

4.- (a) P. Horcajada, R. Gref, T. Baati, P. K. Allan, G. Maurin, G. Férey, R. Morris and C. Serre, *Chem. Rev.*, 2012, **112**, 1232. (b) I. Abánades Lázaro and R. S. Forgan, *Coord. Chem. Rev.*, 2019, **380**, 230.

5.- J. Liu, L. Chen, H. Cui, J. Zhang, L. Zhang and C. Y. Su, *Chem. Soc. Rev.*, 2014, **43**, 6011.

6.- (a) J. Cepeda, S. Pérez-Yáñez, G. Beobide, O. Castillo, E. Goikolea, F. Aguesse, L. Garrido, A. Luque and P. A. Wright, *Chem. Mater.*, 2016, **28**, 2519. (b) K. Fujie, R. Ikeda, K. Otsubo, T. Yamada and S. Kitagawa, *Chem. Mater.*, 2015, **27**, 7355.

7.- (a) Y. Inokuma, S. Yoshioka, J. Ariyoshi, T. Arai, Y. Hitora, K. Takada, S. Matsunaga, K. Rissanen and M. Fujita, *Nature*, 2013, **465**, 461. (b) C. Wang, D. Liu and W. Lin, *J. Am. Chem. Soc.*, 2013, **135**, 13222.

8.- (a) K. Binnemans, *Chem. Rev.*, 2009, **109**, 4283. (b) M. D. Allendorf, C. A. Bauer, R. K. Bhaktaa and R. J. T. Houk, *Chem. Soc. Rev.*, 2009, **38**, 1330. (c) G. Minguez Espallargas and E. Coronado, *Chem. Soc. Rev.*, 2018, **47**, 533. (d) M. Murrie, *Chem. Soc. Rev.*, 2010, **39**, 1986. (e) S. Gómez-Coca, D. Aravena, R. Morales and E. Ruiz, *Coord. Chem. Rev.*, 2015, **289**, 379.

9.- (a) R. Vincent, S. Klyatskaya, M. Ruben, W. Wernsdorfer and F. Balestro, *Nature*, 2012, **488**, 357. (b) M. Ganzhorn, S. Klyatskaya, M. Ruben and W. Wernsdorfer, Nat. *Nanotechnol.*, 2013, **8**, 165. (c) M. Prezioso, A. Riminucci, P. Graziosi, I. Bergenti, R. Rakshit, R. Cecchini, A. Vianelli, F. Borgatti, N. Haag, M. Willis, A. J. Drew, W. P. Gillin and V. A. Dediu, *Adv. Mater.*, 2013, **25**, 534. (d) R. Sessoli, M.-E. Boulon, A. Caneschi, M. Mannini, L. Poggini, F. Wilhelm and A. Rogalev, *Nat. Phys.*, 2015, **11**, 69.

10.- (a) E. San Sebastian, A. Rodríguez-Diéguez, J. M. Seco, J. Cepeda, *Eur. J. Inorg. Chem.*, 2018, 2155. (b) C. Murawski, K. Leo, M. C. Gather, *Adv. Mater.* **2013**, *25*, 6801. (c) M. Gutiérrez, C. Martin, K. Kennes, J. Hofkens, M. Van der

ARTICLE

Auweraer, F. Sánchez and A.Douhal, *Adv. Opt. Mater.*, 2018, **6**, 1870022.

11.- (a) F.-Y. Yi, D. Chen, M.-K. Wu, L. Han and H.-L. Jiang, *ChemPlusChem*, 2016, **81**, 675–690. (b) Z. Hu, B. J. Deibert and J. Li, *Chem. Soc. Rev.*, 2014, **43**, 5815.

12.- (a) N. N. Greenwood and A. Earnshaw, Chemistry of the elements (2nd ed.), Butterworth-Heinemann, 1997, pp. 1230. (b) R. A. Layfield, M. Murugesu (eds), *Lanthanides and Actinides in Molecular Magnetism*, Wiley-VCH, Weinheim, Germany, 2015. (c) B. W. Wang, S. Gao, *The Rare Earth Elements Fundamental and Applications,* D. A. Atwood, John Wiley and sons, 2012.

13.- J. J. Baldoví, E. Coronado, A. Gaita-Ariño, C. Gamer, M. Giménez-Marqués and G. Mínguez-Espallargas, *Chem.–Eur. J.*, 2014, **20**, 10695–10702.

14.- (a) D. N. Woodruff, R. E. P. Winpenny and R. A. Layfield, *Chem. Rev.*, 2013, **113**, 5110. (b) R. Sessoli and A. K. Powell, *Coord. Chem. Rev.*, 2009, **253**, 2328.

15.- F.-S. Guo, B. M. Day, Y.-C. Chen, M.-L. Tong, A. Mansikkamäki, R. A. Layfield, *Science*, 2018, **362**, 1400.

16.- (a) J. C. G. Bünzli, C. Piguet, *Chem. Soc. Rev.*, 2005, **34**, 1048. (b) D. Parker, *Chem. Soc. Rev.*, 2004, **33**, 156. (c) J. Heine, K. Müller-Buschbaum, *Chem. Soc. Rev.*, 2013, **42**, 9232.

17.- (a) Y.-W. Yip, H. Wen, W.-T. Wong, P. A. Tanner and K.-L. Wong, *Inorg. Chem.*, 2012, **51**, 7013. (b) D. E. Barry, D. F. Caffrey and T. Gunnlaugsson, *Chem. Soc. Rev.*, 2016, **45**, 3244.

18.- J. M. Seco, I. Oyarzabal, S. Pérez-Yáñez, J. Cepeda, A. Rodríguez-Diéguez, *Inorg. Chem.*, 2016, **55**, 11230.

19.- W. Liu and X. Tang, *Struct. Bond*, 2015, **163**, 29.

20.- (a) B. Kesanli and W. Lin, *Coord. Chem. Rev.*, 2003, **246**, 305. (b) G. Ferey, *Chem. Soc. Rev.*, 2008, **37**, 191. (c) T. Verbiest, S. V. Elshocht, M. Kauranen, L. Hellemans, J. Snauwaert, C. Nuckolls, T. J. Katz and A. Persoons, *Science*, 1998, **282**, 913.

21.- (a) R. Farshchi, M. Ramsteiner, J. Herfort, A. Tahraoui, H. T. Grahn, *Appl. Phys. Lett.*, 2011, **98**, 162508. (b) I. Žutić, J. Fabian and S. Das Sarma, *Rev. Mod. Phys.*, 2004, **76**, 323.

22.- (a) C. Wagenknecht, C.-M. Li, A. Reingruber, X.-H. Bao, A. Goebel, Y.-A. Chen, Q. Zhang, K. Chen, J.-W. Pan, *Nat. Photon.*, 2010, **4**, 549. (b) J. F. Sherson, H. Krauter, R. K. Olsson, B. Julsgaard, K. Hammerer, I. Cirac and E. S. Polzik, *Nature*, 2006, **443**, 557.

23.- C. Wang, H. Fei, Y. Qiu, Y. Yang, Z. Wei, Y. Tian, Y. Chen, Y. Zhao, *Appl. Phys. Lett.*, 1999, **74**, 19.

24.- (a) T. Oka, H. Aoki, *Phys. Rev. B*, 2009, **79**, 081406. (b) Y. H. Wang, H. Steinberg, P. Jarillo-Herrero, N. Gedik, *Science*, 2013, **342**, 453.

25.- Y. Yang, R. C. da Costa, M. J. Fuchter and A. J. Campbell, *Nat. Photonics,* 2013, **7**, 634.

26.- T. Novikova, A. Pierangelo, A. De Martino, A. Benali and P. Validire, *Opt. Photonics News,* 2012, 26.

27.- (a) M. Wakabayashi, S. Yokojima, T. Fukaminato, K.-I. Shiino, M. Irie and S. Nakamura, *J. Phys. Chem. A*, 2014, **118**, 5046. (b) S. Abbate, F. Lebon, G. Longhi, M. Passarello and V. T. Liveri, *Chirality*, 2011, **23**, 910. (c) T. Mori, S. Grimme and Y. Innoue, *J. Org. Chem.*, 2007, **72**, 6998.

28.- S.-M. Chen, L.-M.Chang, X.-K. Yang, T. Luo, H. Xu, Z.-G. Gu, J. Zhang, *ACS Applied Materials & Interfaces*, 2019, **11**, 31421.

29.- (a) R. Carr, N. H. Evans and D. Parker, *Chem. Soc. Rev.*, 2012, **41**, 7673. (b) G. Bozoklu, C. Gateau, D. Imbert, J. Pécaut, K. Robeyns, Y. Filinchuk, F. Memon, G. Muller and M. Mazzanti, *J. Am. Chem. Soc.*, 2012, **134**, 8372.

30.- (a) L. H. G. Kalinke, C. Cangussu, M. Mon, R. Bruno, E. Tiburcio, F. Lloret, D. Armentano, E.Pardo and J. Ferrando-Soria, *Inorg. Chem.*, 2019, **58**, 14498. (b) Y. Guo, L. Zhang, N. Muhammad, Y. Xu, Y. Zhou,F. Tang and S. Yang, *Inorg. Chem.*, 2018, **57**, 995.

31.- E. Coronado, J. R. Galán-Mascarós, C. J. Gómez-García and A. Murcia-Martínez, *Chem.–Eur. J.*, 2006, **12**, 3484.

32.- (a) Shannon, R. D. *Acta Crystallogr.*, 1976, **A32**, 751. (b) E. A. Quadrelli, *Inorg. Chem.*, 2002, **41**, 167.

33.- M. Llunell, D. Casanova, J. Cirera, J. M. Bofill, P. Alemany, S. Alvarez, M. Pinsky, D. Avnir, SHAPE v1.1b, Barcelona (Spain), 2005.

34.- (a) TOPOS: http://www.topos.ssu.samara.ru. (b) V. A. Blatov, M. O'Keeffe and D. M. Proserpio, *CrystEngComm*, 2010, **12**, 44. (c) V. A. Blatov, A. P. Shevchenko and D. M. Proserpio, *Cryst. Growth Des.*, 2014, **14**, 3576.

35.- A. L. Spek, *Acta Cryst.*, 2009, **D65**, 148.

36.- (a) L. Sorace, C. Benelli and D. Gatteschi, *Chem. Soc. Rev.*, 2011, **40**, 3092. (b) P. Díaz-Gallifa, O. Fabelo, J. Pasán, L. Cañadillas-Delgado, F. Lloret, M. Julve and C. Ruiz-Pérez, *Inorg. Chem.* **2014**, *53*, 6299.

37.- (a) D. Aguilà, L. A. Barrios, V. Velasco, L. Arnedo, N. Aliaga-Alcalde, M. Menelaou, S. J. Teat, O. Roubeau, F. Luis and G. Aromí, *Chem.–Eur. J.* **2013**, *19*, 5881. (b) N. W. Waggoner, B. Saccoccia, I. A. Ibarra, V. M. Lynch, P. T. Wood and S. M. Humphrey, *Inorg. Chem.* **2014**, *53*, 12674.

38.- J. Cepeda, R. Balda, G. Beobide, O. Castillo, J. Fernández, A. Luque, S. Pérez-Yáñez, P. Román and D. Vallejo-Sánchez, *Inorg. Chem.*, 2011, **50**, 8437.

39.- (a) L. Cañadillas-Delgado, T. Martín, O. Fabelo, J. Pasán, F. S. Delgado, F. Lloret, M. Julve, C. Ruiz-Pérez, *Chem.–Eur. J.*, 2010, **16**, 4037. (b) L. Cañadillas-Delgado, O. Fabelo, J. Pasán, F. S. Delgado, F. Lloret, M. Julve, C. Ruiz-Pérez, *Dalton Trans.*, 2010, 7286.

40.- J. Ruiz, A.J. Mota, A. Rodríguez-Diéguez, S. Titos, J.M. Herrera, E. Ruiz, E. Cremades, J.P. Costes, J. Colacio, *Chem. Commun.*, 2012, **48**, 7916.

41.- N. Ishikawa, M. Sugita, T. Ishikawa, S.-y Koshihara, Y. Kaizu, *J. Am. Chem. Soc.*, 2003, **125**, 8694.

42.- (a) F.-S. Guo, B. M. Day, Y.-C. Chen, M. Liang-Tong, A. Mansikkamäki, R. A. Layfield, *Angew. Chem. Int. Ed.*, 2017, **56**, 11445. (b) C. A. P. Goodwin, F. Ortu, D. Reta, N. F. Chilton, D. P. Mills, *Nature*, 2017, **548**, 439. (c) S.-D. Jiang, B.-W. Wang, H.-L Sun, Z.-M. Wang, S. Gao, *J. Am. Chem. Soc.*, 2011, **133**, 4730. (d) Y.-S. Ding, T. Han, Y.-Q. Zhai, D. Reta, N. F. Chilton, R. E. Winpenny, Y.-Z. Zheng, *Chem.-Eur. J.*, 10.1002/chem.202000646

43.- P. Antal, B. Drahoš, R. Herchel, Z. Trávníček, *Dalton Trans.*, 2016, **45**, 15114.

44.- A. Singh, K. N. Shrivastava, *Phys. Status Solidi*, 1979, **95**, 273.

45.- N. F. Chilton, CCFIT program, The Chilton Group, Manchester,

ARTICLE

U.K., 2014, http://www.nfchilton.com/software.html.

46.- (a) R. C. Evans, P. Douglas, C. J. Winscom, *Coord. Chem. Rev.,* 2006, **250**, 2093. (b) Q. -D. Liu, R. Wang, S. Wang, *Dalton Trans.*, 2004, 2073. (c) J. Rocha, C. D. S. Brites, L. D. Carlos, *Chem. Eur. J.*, 2016, **22**, 14782.

47.- (a) K. Binnemans, *Chem. Rev.*, 2009, **109**, 4283. (b) J. C. G. Bünzli, *Coord. Chem. Rev.*, 2015, **293-294**, 19.

48.- (a) B. C. Jamalaiah and Y. R. Babu, *Mat. Chem. Phys.*, 2018, **211**, 181. (b) Z. Y. Mao, Y. C. Zhu, L. Gan, Y. Zeng, F. F. Xu, Y. Wang, H. Tian, J. Li and D. J. Wang, *J. Lumin.*, 2013, **134**, 148. (c) B. Y. Huang, B. L. Feng, L. Luo, C. L. Han, Y. T. He and Z. R. Qiu, *Mater. Sci. Eng. B,* 2016, **212**, 71.

49.- W. M. Yen, S. Shionoya, H. Yamamoto, in Phosphor Handbook, CRC Press, Athens, 2007.

50.- (a) E. Echenique-Errandonea, I. Oyarzabal, J. Cepeda, E. San Sebastian, A. Rodríguez-Diéguez, J. M. Seco, *New J. Chem.*, 2017, **41**, 5467. (b) S. Biju, N. Gopakumar, J.-C. G. Bunzli, R. Scopelliti, H. K. Kim, M. L. P. Reddy, *Inorg. Chem.*, 2013, **52**, 8750.

51.- M. Latva, H. Takalo, V. M. Mukkala, C. Matachescu, J. C. Rodriguez-Ubis, J. Kanakare, *J. Lumin.*, 1997, **75**, 149.

52.- (a) P. C. R. Soares-Santos, L. Cunha-Silva, F. A. Almeida-Paz, R. A. S. Ferreira, J. Rocha, L. D. Carlos, H. I. S. Nogueira, *Inorg. Chem.*, 2010, **49**, 3428. (b) J. Cepeda, S. Pérez-Yáñez, G. Beobide, O. Castillo, J. A. García, M. Lanchas, A. Luque, *Dalton Trans.*, 2015, **44**, 6972. (c) A. de Bettencourt-Dias, P. S. Barber, S. Viswanathan, D. T. de Lill, A. Rollett, G. Ling, S. Altun, *Inorg. Chem.*, 2010, **49**, 8848.

53.- Phosphor Handbook, ed. W. M. Yen, S. Shionoya, H. Yamamoto, CRC Press, Boca Raton, 2007.

54.- A. Beeby, I. M. Clarkson, R. S. Dickins, S. Faulkner, D. Parker, L. Royle, A. S. de Sousa, J. A. Gareth Williams and M. Woods, *J. Chem. Soc. Perkin Trans.*, 1999, **2**, 493.

55.- S. Thushari, J. A. K. Cha, H. H.-Y. Sung, S. S.-Y. Chui, A. L.-F. Leung, Y.-F. Yen and I. D. Williams, *Chem. Commun.*, 2005, 5515.

56.- F. Zinna, and L. Di Bari, *Chirality*, 2015, **27**, 1.

57.- C. K. Luk and F. S. Richardson, *J. Am. Chem. Soc.*, 1975**, 97**, 6666.

58.- (a) C. K. Luk and F. S. Richardson, *Chem Phys. Lett.*, 1974, **25**, 215. (b) M. Seitz, E. G. Moore, A. J. Ingram, G. Muller and K. N. Raymond, *J. Am. Chem. Soc.*, 2007, **129**, 15468. (c) A. P. S. Samuel, J. L. Lunkley, G. Muller and K. N. Raymond, *Eur. J. Inorg. Chem.*, 2010, 3343. (d) L. VandenElzen and T. A. Hopkins, *ACS Sustainable Chem. Eng.*, 2019, **7**, 16690.

59.- (a) M. Seitz, K. Do, A. J. Ingram, E. G. Moore, G. Muller and K. N. Raymond, *Inorg. Chem.*, 2009, **48**, 8469.

60.- (a) P. Yan, J. Xing, G. Li, W. Sun, J. Zhang and G. Hou, *J. Coord. Chem.*, 2009, **62**, 2095. While these (Yan et al.[60] and Thushari et al.[55]) described previously the structural properties of D enantiomers only for the Tb(III) and Dy(III) based MOFs, we herein provide a complete structural description (see SI) of 3D arrangement of both D- and L-enantiomers for all compounds (Tb-Tm).

61.- (a) G. M. Sheldrick, SHELX-2014, Program for Crystal Structure Refinement, University of Göttingen, Göttingen, Germany, 2014. (b) L. J. Farrugia, *J. Appl. Cryst.*, 1999, **32**, 837.

62.- M. J. Frisch, G. W. Trucks, H. B. Schlegel, G. E. Scuseria, M. A. Robb, J. R. Cheeseman, G. Scalmani, V. Barone, B. Mennucci, G. A. Petersson, H. Nakatsuji, M. Caricato, X. Li, H. P. Hratchian, A. F. Izmaylov, J. Bloino, G. Zheng, J. L. Sonnenberg, M. Hada, M. Ehara, K. Toyota, R. Fukuda, J. Hasegawa, M. Ishida, T. Nakajima, Y. Honda, O. Kitao, H. Nakai, T. Vreven, J. A. Montgomery Jr., J. E. Peralta, F. Ogliaro, M. Bearpark, J. J. Heyd, E. Brothers, K. N. Kudin, V. N. Staroverov, R. Kobayashi, J. Normand, K. Raghavachari, A. Rendell, J. C. Burant, S. S. Iyengar, J. Tomasi, M. Cossi, N. Rega, J. M. Millam, M. Klene, J. E. Knox, J. B. Cross, V. Bakken, C. Adamo, J. Jaramillo, R. Gomperts, R. E. Stratmann, O. Yazyev, A. J. Austin, R. Cammi, C. Pomelli, J. W. Ochterski, R. L. Martin, K. Morokuma, V. G. Zakrzewski, G. A. Voth, P. Salvador, J. J. Dannenberg, S. Dapprich, A. D. Daniels, O. Farkas, J. B. Foresman, J. V. Ortiz, J. Cioslowski and D. J. Fox, Gaussian 09, revision A.02, Gaussian, Inc., Wallingford, CT, 2009.

63.- (a) A. D. Becke, *J.* Chem*. Phys.*, 1993, **98**, 5648. (b) B. Miehlich, A. Savin, H. Stoll and H. Preuss, *Chem. Phys. Lett.*, 1989, **157**, 200. (c) C. Lee, W. Yang, R. G. Parr, *Phys. Rev. B*, 1988, **37**, 785.

64.- (a) V. A. Rassolov, M. A. Ratner, J. A. Pople, P. C. Redfern, L. A. Curtiss, *J. Comput. Chem.*, 2001, **22**, 976. (b) M. M. Francl, W. J. Pietro, W. J. Hehre, J. S. Binkley, D. J. DeFrees, J. A. Pople and M. S. Gordon, *J. Chem. Phys.*, 1982, **77**, 3654. (c) P. C. Hariharan and J. A. Pople, *Mol. Phys.*, 1974, **27**, 209.